Noname manuscript No.
(will be inserted by the editor)

On the anatomical definition of arterial networks in blood flow simulations: comparison of detailed and simplified models

Pablo J. Blanco · Lucas O. Müller · Sansuke M. Watanabe · Raúl A. Feijóo

Received: date / Accepted: date

Abstract The goal of this work is to assess the impact of vascular anatomy definition degree in the predictions of blood flow models of the arterial network. To this end, results obtained with an anatomically detailed network containing over 2000 vessels are systematically compared with those obtained with an anatomically simplified network containing the main 86 vessels, the latter being a truncated version of the former one. The comparison is performed quantitatively and qualitatively in terms of pressure and flow rate waveforms, wave intensity analysis and impedance analysis. Comparisons are performed under physiological conditions and for the case of common carotid artery occlusion. Mechanisms of blood flow delivery to the brain, as well as different blood flow steal phenomena, are unveiled on the light of model predictions. Results show that detailed and simplified models are in reasonable agreement regarding the hemodynamics in larger vessels and in healthy scenarios. The anatomically detailed arterial network features improved predictive capabilities at peripheral vessels. Moreover, discrepancies between models are substantially accentuated in the case of anatomical variations or abnormal hemodynamic conditions. We conclude that physiologically meaningful agreement between models is obtained for normal hemodynamic conditions. This agreement rapidly deteriorates for abnormal blood flow conditions such as those caused by total arterial occlusion. Differences are even larger when modifications of the vascular anatomy are considered. This rational comparison allows us to gain insight into the need for anatomically detailed arterial networks when addressing complex hemodynamic interactions.

Keywords Blood flow, wave propagation, arterial function, carotid occlusion, carotid steal.

P.J. Blanco · R.A. Feijóo
Laboratório Nacional de Computação Científica,
Av. Getúlio Vargas 333, Petrópolis, 25651-075, Brazil
S.M. Watanabe
Federal Rural University of Pernambuco, Av. Bom Pastor, s/n, Boa Vista, Garanhuns-PE 55292-270, Brazil
L.O. Müller
Department of Mathematics, University of Trento, via Sommarive, 14, Trento 38123 Povo, Italy
Tel.: +55-24-22336067
Fax: +55-24-22336071
E-mail: pjblanco@lncc.br

P.J. Blanco · L.O. Müller · S.M. Watanabe · R.A. Feijóo
National Institute of Science and Technology in Medicine Assisted by Scientific Computing, INCT-MACC, Petrópolis, Brazil

1 Introduction

One-dimensional (1D) modeling is the preferred approach to study blood flow at the level of the entire circulation because of its low computational cost and widely demonstrated predictive capabilities. Throughout the last decades several descriptions of the arterial network have been reported in the specialized literature, addressing a comprehensive range of cardiovascular problems, from basic research to clinical applications Matthys et al (2007); Mynard and Nithiarasu (2008); Stergiopulos et al (1992); Ho et al (2012).

Remarkably, the aforementioned works adopted anatomically simplified arterial topologies to describe hemodynamic phenomena in the arterial network with little debate about validity and related implications of the truncation of the network when modeling peripheral hemodynamics and disease, as well as abnormal conditions. In the last years, research started to focus in the refinement of anatomical detail to improve the predictive capabilities of models. Taking into account

contributions dealing with, at least, the entire arterial system, in Reymond et al (2009) the description of the cerebral arterial network was improved adding the circle of Willis. Also, in Alastruey et al (2007); Koeppl et al (2014); Liang et al (2011), 1D models incorporating the circle of Willis were employed to study carotid artery stenosis, and Perdikaris et al (2015) addressed the extension of vascular trees through fractal networks as a strategy to construct boundary conditions. Likewise, in Guan et al (2016) the authors studied the impact of modeling peripheral beds as structured trees Olufsen et al (2000), in contrast to standard Windkessel models. In Müller and Toro (2014a,b) the arterio-venous coupling was addressed with special emphasis in the cerebral circulation to analyze the hemodynamic effect of stenotic venous vessels. A further closed-loop representation of the circulation was reported in Mynard and Smolich (2015).

A common feature of all these contributions is a lack of discussion about the impact of the truncation of the arterial (or venous) network. In order to provide a representation closer to anatomical reality, enabling the study of blood flow phenomena in anatomically realistic conditions, in Blanco et al (2014, 2015) an *Anatomically Detailed Arterial Network* (ADAN) model was constructed. The outstanding feature of the ADAN model is that it contains almost all arterial vessels which are acknowledged by the specialized literature according to classical anatomy textbooks Dauber (2007); Netter (2011). The criterion to define the arterial topology was the following: *if the artery has a name and a visual reference in Dauber (2007); Netter (2011), it is contained in the model*. Some preliminary results reported in Blanco et al (2015) provide clear evidence of how misleading it could be to simulate disease conditions using anatomically simplified network models. The ADAN model was employed in Blanco et al (2016) to study subclavian steal phenomena, and in Blanco et al (2017) to study the interplay between hypertension and cerebral small vessel disease. Moreover, the ADAN model constituted the baseline arterial model to build a reduced model, called ADAN-86, featuring 86 arterial vessels which has been made available to the research community Safaei et al (2016), and also has been used as the reference solution for the setting of bond-graph models of the cerebral circulation in Safaei et al (2018).

Noteworthy, in Epstein et al (2015), a 1D model of the arterial system including 55 large arterial vessels is compared with truncated versions of the very same network by systematically trimming downstream vessels and turning them into equivalent Windkessel models in some defined sense. The study reports a quantitative comparison that allows us to understand the impact of severe truncation of arterial networks in blood flow simulations for different cardiovascular scenarios. Thus, the present work can also be interpreted as a study following the approach of Epstein et al (2015), for the ADAN model is compared with its truncated version, the ADAN-86. Also, in Fossan et al (2018) a strategy for optimizing terminal parameters is proposed to maintain accuracy of truncated networks when compared to a more refined (reference) network of 96 arteries. In contrast to Epstein et al (2015) and to the present work, the lumping strategy requires the solution of the refined model.

The goal of the present work is to scrutiny the relevance of the anatomical definition degree in 1D blood flow simulations. Specifically, the level of agreement and discrepancy in predictions delivered by the ADAN model and by a truncated 86-vessel network, hereafter called ADAN-86 model, see Safaei et al (2016), are studied in depth in order to critically examine the predictive and descriptive capabilities of such networks in normal and abnormal scenarios of vascular anatomy. Differences in results obtained with both models are illustrated by means of comparison of pressure and flow rate waveforms, arterial impedance analysis and wave intensity analysis. The case of abnormal vascular anatomy is represented by a scenario featuring a total common carotid occlusion. Such situation can be found either in surgical procedures Ouriel et al (2001) or in the presence of an extremely severe stenosis. From the modeling point of view, this condition is particularly challenging because it triggers complex hemodynamic forces that lead to different *steal* phenomena between intracranial and extracranial vasculatures, as well as between cerebral hemispheres, with the circle of Willis playing a major role in redistributing blood flow to distal territories.

2 Methods

2.1 Mathematical model

Blood flow is modeled using classical 1D equations to describe flow rate Q, lumen area A and blood pressure P in the space-time domain, namely

$$\frac{\partial A}{\partial t} + \frac{\partial Q}{\partial x} = 0, \tag{1}$$

$$\frac{\partial Q}{\partial t} + \frac{\partial}{\partial x}\left(\frac{Q^2}{A}\right) = -\frac{A}{\rho}\frac{\partial P}{\partial x} - \frac{8\pi\mu}{\rho A}Q, \tag{2}$$

where ρ and μ are blood density and viscosity, respectively. The behavior of the arterial wall is described by the following constitutive equation incorporating elastin,

collagen and smooth muscle contributions Blanco et al (2015); Urquiza et al (1995)

$$P = P_o + \frac{\pi h r_o}{A}\left[E_E\varepsilon + \ E_C\epsilon_r \ln(\mathrm{e}^u + 1) + K_M\dot{\varepsilon}\right], \quad (3)$$

with $\varepsilon = \sqrt{\frac{A}{A_o}} - 1$ (therefore $\dot{\varepsilon} = \frac{\dot{A}}{2\sqrt{AA_o}}$), $u = \frac{\varepsilon-\varepsilon_0}{\epsilon_r}$, where r is the lumen radius, $A = \pi r^2$ (r_o, A_o are reference values at pressure $P_o = 1{\cdot}10^5$ dyn/cm^2, which is of the order of the diastolic pressure), h is the arterial wall thickness, E_E, E_C and K_M are effective moduli for the elastin, collagen and viscoelastic components, respectively. Finally, ε_0 and ϵ_r model the fiber recruitment through the localization and width of the distribution of the fiber strain activation.

To determine effective material properties we considered W_E, W_C, W_M to be the volume fractions of elastin, collagen and smooth muscle, respectively (i.e. $W_E{+}W_C{+}W_M = 1$), and, through the rule of mixtures, we get

$$E_E = W_E E_E, \quad E_C = W_C E_C, \quad K_M = W_M K_M, \quad (4)$$

where E_E, E_E and K_M are the material properties of individual components (values reported in Table 1). Parameter E_E was taken from Avolio (1980), collagen parameters $E_C, \varepsilon_0, \epsilon_r$ were determined inspired by the data published by Weizsacker and Pinto (1988). The viscoelastic parameter K_M was determined such that hysteresis loops in peripheral arteries are within the physiological range Armentano et al (1991).

Parameter	Value
E_E [dyn/cm^2]	$4 \cdot 10^6$
E_C [dyn/cm^2]	$1 \cdot 10^9$
ε_0	0.35
ϵ_r	0.05
K_M [dyn s/cm^2]	$3 \cdot 10^5$

Group	r_o [cm]
A	$r_o > 0.18$
B	$0.07 \leq r_o \leq 0.18$
C	$0.07 \geq r_o$

Group	A	B	C
W_E	0.9	0.7	0.45
W_C	0.099	0.25	0
W_M	0.001	0.05	0.55

Table 1 Top left: Values of material properties for the arterial wall. Top right: Clusterization of arterial vessels according to the lumen radius r_o. Bottom: Volume fractions for elastin, collagen and smooth muscle for the different clusters.

Arterial vessels were clustered according to the lumen radius into three groups as described in Table 1 based on the change of material properties observed in cerebral vessels Godlevska et al (1974), and based on the extremely muscular character of pre-arteriolar vessels. Volume fractions W_E, W_C and W_M were determined through the following qualitative guidelines Burton (1954); Godlevska et al (1974): large arteries (group A) are dominantly elastic; mid-sized arteries (group B) have more collagen content than large arteries, they have less elastin content than large arteries, and also have more smooth muscle than large arteries; small arteries (group C) are dominantly muscular, and they have less elastin content than larger arteries. The final values have been defined using a sensitivity analysis to study the impact on the model response, and are reported in Table 1. This combination of parameters is the one used in Blanco et al (2015), and is one parameter set that proved to be effective in terms of predictive capabilities.

An inflow function, taken from Mynard and Smolich (2015), is prescribed at the root of the aorta in both models, see Figure 1. Terminal arterial segments are modeled as Windkessel elements

$$R_A R_B C\frac{dQ}{dt} = R_B C\frac{d}{dt}(P{-}P_T){+}(P{-}P_T){-}(R_A{+}R_B)Q, \quad (5)$$

where P_T is a reference terminal pressure, C is the peripheral compliance and R_A and R_B are resistive elements.

Numerical solution of the system of equations (1)-(2)-(3) is accomplished using the local time-stepping finite volume numerical scheme described in Müller et al (2016) where full details about the coupling of 1D domains, the prescription of boundary conditions and the discretization of the above presented models are provided. In all cases, ten cardiac cycles are simulated to ensure that a periodic state is achieved, and the reported results are those from the last cycle.

2.2 Derived hemodynamic quantities

After solving the system of equations (1)-(2)-(3), different cardiovascular indexes that characterize the arterial function such as the ankle-brachial index, pulse pressure amplification, pulse wave velocity and wave intensity (see also Section 2.5 below) are computed. The definition of these indexes is summarized in Blanco et al (2015).

2.3 Arterial networks and study cases

This section presents the arterial networks employed in the analysis. Both networks are displayed in Figure 1.

2.3.1 Anatomically detailed network

The ADAN model was developed in compliance with classical anatomy textbooks Dauber (2007); Netter (2011).

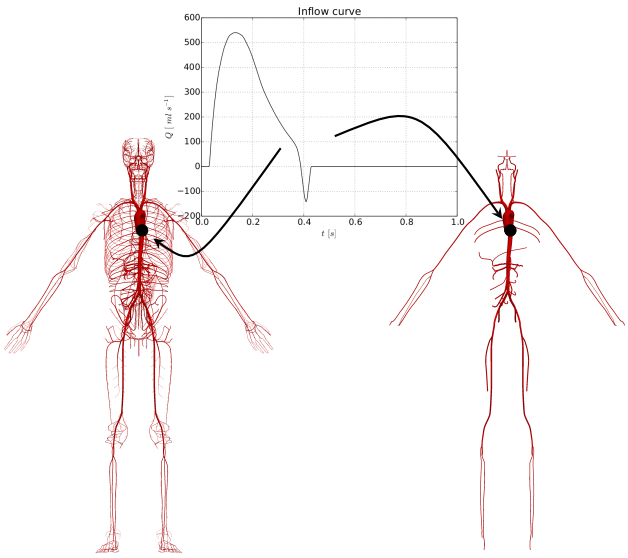

Fig. 1 Inflow condition prescribed to models: ADAN (left) and ADAN-86 (right).

Parameter/Model	ADAN	ADAN-86
HR [bpm]	60	60
CO [cm^3/s]	112.0	112.0
R_P [dyn s/cm^5]	1030.8	1177.6
C_P [10^{-5} cm^5/dyn]	6.75	27.02
τ_i [ms], $\forall i$	64.2	256.9
(DBP-SBP) [10^4 dyn/cm^2]	(10.42-14.86)	(10.24-15.06)
(DBP-SBP) [mmHg]	(78.21-111.46)	(76.83-112.92)
ABI	1.13	1.05
PPA	1.16	1.04
PWV_{AF} [cm/s]	650	679
PWV_{CF} [cm/s]	601	632

Table 2 Global model data and selected cardiovascular parameters given by the ADAN and the ADAN-86. HR: heart rate, CO: cardiac output, R_P: total peripheral resistance, C_P: total peripheral compliance, $\tau_i = R_{B_i} C_i$: characteristic time constant for terminal i, SBP: systolic blood pressure (aortic root), DBP: diastolic blood pressure (aortic root), ABI: ankle-brachial index. PPA: pulse pressure amplification (brachial minus aortic root pressure pulse). PWV: pulse wave velocity. Subscripts (arteries): A: ascending aorta (proximal point), C: common carotid (distal point), F: femoral (distal point).

It comprises 2142 arterial vessels, 1598 of which have a well acknowledged name according to the International Anatomical Terminology Dauber (2007), and 544 are perforator vessels. Note that a single vessel is actually composed by more than one 1D segment, with a total of 4041 segments. The vasculature supplies blood to 28 specific organs (kidneys, liver, brain, glands, etc.) and to 116 vascular territories which altogether form the distributed organs (bones, muscles, skin, nerves). Such extremely detailed description of peripheral beds provides a connection between the definition of outflow boundary conditions and the morphometry of vascular territories. For a detailed description of the blood flow distribution criteria used in the model, the interested reader is directed to Blanco et al (2014), while the definition of model parameters, a sensitivity analysis and a comparison against in-vivo data are reported in Blanco et al (2015). Also, a web application with a user-friendly interface to interact with the dataset is openly available in HeMoLab (2013). General data for the model setting are presented in Table 2.

For the present study, the ADAN model was further enriched by adding collateral vessels existing around the thyroid gland, following the anatomical guidelines reported in Jianu et al (2009). Specifically, a thyroid arterial plexus was added to the model, as these pathways are believed to play an important role in the blood flow supply to the head in cases of carotid occlusive disease Jianu et al (2009); Dorrance (1934); Ozbek et al (1998). The detailed modifications to the original ADAN model are reported in Blanco et al (2016).

2.3.2 Anatomically simplified network

The simplified version of the ADAN model was conceived ensuring that most frequently used arterial vessels encountered in previous descriptions of the arterial network are present Stergiopulos et al (1992); Alastruey et al (2014); Wang and Parker (2004). This truncated version contains 86 arterial vessels including the Circle of Willis (CoW), and was reported in Safaei et al (2016). The material parameters involved in the tube law (3) are the same ones used for ADAN. See Table 2 for global parameters that characterize the ADAN-86 model. Anatomical simplification implies removing vascular territories and minor organs. The cardiac output (total inflow denoted by Q_T) used here is the same as in ADAN. Terminal resistances are computed following three criteria (see Table 3):

– *Criterion I.* Blood supply to major specific organs is maintained invariant with respect to ADAN. Resistances of terminal vessels in these vessels are computed as follows: Let $Q^I = \frac{\mathrm{BF}}{100} Q_T$ be the flow to the specific organ, with BF being the percentage of cardiac output directed to the organ (see Table 3). The total organ resistance, assuming a reference pressure P_{ao}, is $R^I = \frac{P_{\mathrm{ao}}}{Q^I}$. Let m be the number of vessels supplying a given organ, the flow supplied by terminal vessel i is determined by Murray's law, and so the total Windkessel resistance is

$$R^I_{T,i} = \alpha_i \frac{P_{\mathrm{ao}}}{Q^I} \quad \alpha_i = \frac{r^3_{o,i}}{\sum_{j=1}^{m} r^3_{o,j}}. \tag{6}$$

– *Criterion II.* Blood to extracranial territories through the external carotid artery and to part of the intercostal space, through intercostal vessels are such that these arteries carry the same blood as in ADAN. Let Q_i^{ADAN} be the flow supplied by vessel i, as given by the simulation with ADAN. The total Windkessel resistance of that vessel in ADAN-86 is

$$R_{T,i}^{II} = \frac{P_{\text{ao}}}{Q_i^{\text{ADAN}}}. \tag{7}$$

Note that this data from the refined model is only required to make both simulations comparable in terms of flow rate transported by these vessels.

– *Criterion III.* The vessels that supply the upper and lower limbs carry the extra flow rate such that the total flow rate is Q_T. Let Q_i^{ADAN} be the flow supplied by vessel i, as given by the simulation with ADAN. The total Windkessel resistance of that vessel in ADAN-86 is

$$R_{T,i}^{III} = \beta_{III} \frac{P_{\text{ao}}}{Q_i^{\text{ADAN}}} \tag{8}$$

where β_{III} is such that the equivalent resistance R_P in ADAN-86 computed as $R_P = \left(\sum_{i=1}^{m_P} \frac{1}{R_{T,i}}\right)^{-1}$ (m_P: number of terminal vessels in ADAN-86) verifies $R_P P_{\text{ao}} = Q_T$ (this value is $\beta_{III} = 0.43$).

Here we considered $P_{\text{ao}} = 100$ mmHg and rescaled all the resistances by a factor $\beta_R = 0.93$ to ensure that the mean pressure at the aortic root in both models was the same. Finally, two strategies were tested to define R_A and R_B in the Windkessel model: first we considered $R_A = 0.2R_T$ and $R_B = 0.8R_T$ (R_T: total Windkessel resistance), second we computed R_A, R_B using the characteristic impedance of the terminal vessel as proposed by Epstein et al (2015). The results reported in this work correspond to the first strategy. Peripheral compliance for vessel i was selected such that the characteristic constants verify $\tau^{\text{ADAN-86}} = \beta_C \tau^{\text{ADAN}}$, where β_C is such that the difference in the pressure pulse SBP − DBP (at the aortic root) between both models remains below 10%, yielding $\beta_C = 4.00$. The characteristic time constant is uniform for all terminal vessels, and is reported in Table 2 for both models.

2.3.3 Study cases

In the present work we are exclusively interested in arterial function. Therefore, it is assumed that the heart behaves as a flow source. The cardiac ejection is thus the same for both models, and it is displayed in Figure 1. First, two scenarios are considered:

Criterion	Organ	BF [%]
I	Encephalon	12.00
I	Liver	6.50
I	Kidney (×2)	9.50
I	Stomach	1.00
I	Pancreas	1.00
I	Spleen	3.00
I	Intestines	13.25
II	Extracranial territories (×2)	2.49
II	Intercostal space	0.20
III	Upper limb (×2)	3.74
III	Lower limb (×2)	15.80

Table 3 Blood flow distribution to major territories for ADAN-86 and criteria used in the definition of peripheral resistances.

(i) Reference scenario → model with the setting presented in Blanco et al (2015), corresponding to a healthy subject, and taking into consideration the additional collateral vessels as already explained in Section 2.3.1;

(ii) Occlusion scenario (w/ACoA) → model characterized by total occlusion of the left common carotid artery; like the reference scenario, this model includes the anterior communicating artery (ACoA).

A further scenario is included to explore the mechanisms of blood flow delivery in extra- and intracranial vessels, specifically:

(iii) Occlusion scenario (wo/ACoA) → idem (ii), but without the ACoA (i.e. an open CoW).

Figure 2 presents the vascular geometry of the tributary vessels of the CoW and the major cerebral vessels.

Cases (ii) and (iii) were chosen to bring to light the mechanisms behind collateral blood supply to the brain and to extracranial territories. As it will be seen, these mechanisms change according to blood-carrying capacity of different collateral pathways Liebeskind (2003), revealing different steal phenomena which can be of interest in clinical practice Ouriel et al (2001).

For the purpose of the analysis involving blood supply to the brain, we consider the set of intracranial vessels to be formed by the tributary vessels of the Circle of Willis, the circle itself and by the arteries that leave the circle, i.e. the anterior, middle and posterior cerebral arteries. Extracranial vessels are those arteries that branch from the external carotid artery as well as from the vertebral artery and that run through the neck, scalp and face without entering the cranium.

2.4 Impedance analysis

To compute the input impedance of the arterial networks under consideration we perform a Fourier trans-

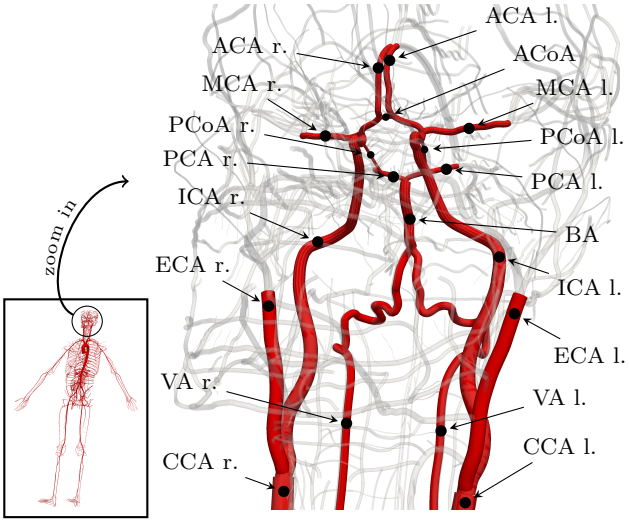

Fig. 2 Tributaries of the Circle of Willis and major vessels feeding the brain. CCA: common carotid artery, ICA: internal carotid artery, ECA: external carotid artery, VA: vertebral artery, BA: basilar artery, MCA: middle cerebral artery, ACA: anterior cerebral artery, PCA: posterior cerebral artery, ACoA: anterior communicating artery, PCoA: posterior communicating artery. l.: left, r.: right.

form of pressure and flow time series at the proximal location of the ascending aorta artery, and thus we obtain the amplitude of the first $N = 14$ harmonics. Once this information is available, the impedance in terms of modulus and phase can be readily computed. The characteristic impedance Z_c, used to normalize the impedance modulus, is computed as the average of impendace moduli for frequencies higher than 2 Hz.

2.5 Wave intensity analysis

We perform a non-linear wave intensity analysis, as proposed in Mynard et al (2012). Neglecting vessel wall viscoelasticity, Riemann invariants of system of equations (1)-(2), can be written as

$$w_\pm = U \pm \int_{P_0}^{P} \frac{1}{\rho c(P')} dP' \,, \tag{9}$$

where $U = \frac{Q}{A}$ is the cross-sectional averaged velocity and $c(P) = \sqrt{\frac{A}{\rho}\frac{\partial P}{\partial A}}$ is the wave speed.

Defining the difference operator d, between two characteristic curves travelling in the same direction, as $df = f(x_2, t_2) - f(x_1, t_1)$, wave intensity is given by

$$dPdU = \rho c(P) \frac{dw_+^2 - dw_-^2}{4} \,. \tag{10}$$

In this work we use the time-corrected version of wave intensity Ramsey and Sugawara (1997), namely

$$dI = \rho c(P) \frac{dw_+^2 - dw_-^2}{4\,\Delta t^2} \,, \tag{11}$$

with $dw_\pm$ computed from (9)

$$dw_\pm = dU \pm \frac{1}{\rho c(P)} dP \,. \tag{12}$$

Manipulations of the above equations, see Mynard et al (2012) for details, result in the following expressions

$$dP_\pm = \pm \frac{\rho c_\pm}{2} dw_\pm \,, \quad dU_\pm = \frac{1}{2} dw_\pm \,. \tag{13}$$

Moreover, the non-linear decomposition of (11) is given by

$$dI_\pm = \pm \frac{\rho c_\pm}{4} \left(\frac{dw_\pm}{\Delta t} \right)^2 \,. \tag{14}$$

Another quantity used in this study is the wave energy

$$E = \int_T dP dU dt \,, \tag{15}$$

where T is the integration period, here taken as the duration of the cardiac cycle.

3 Results

3.1 Healthy condition

Table 2 presents cardiovascular indexes for both models. The variation in these indexes is: ΔDBP = 1.77%, ΔSBP = 1.31%, ΔPPA = 10.47%, ΔABI = 7.27%, $\Delta\text{PWV}_{\text{AF}} = 4.44\%$ and $\Delta\text{PWV}_{\text{CF}} = 5.13\%$ (measured relative to the average between both models).

Pressure and flow rate waveforms at selected vessels are displayed in Figure 3. While systolic pressure predicted by both models in the ascending aorta artery (AoA: aortic arch) is similar, a smooth and more pronounced pressure build-up is appreciated after the dicrotic notch in ADAN-86. Differences tend to increase along the aorta, as seen in the abdominal aorta (AbAo) and in smaller vessels such as the posterior tibial artery (PTA) and the common carotid artery (CCA). At the middle point of the superior mesenteric artery (SMA) ADAN predicts a smaller flow rate than ADAN-86, with different signature. The same comparison holds for the internal iliac artery (IIA), which follows from the fact that blood flow rate excess is sent to upper and lower limbs in ADAN-86. A quantitative analysis highlights other differences as we will see below.

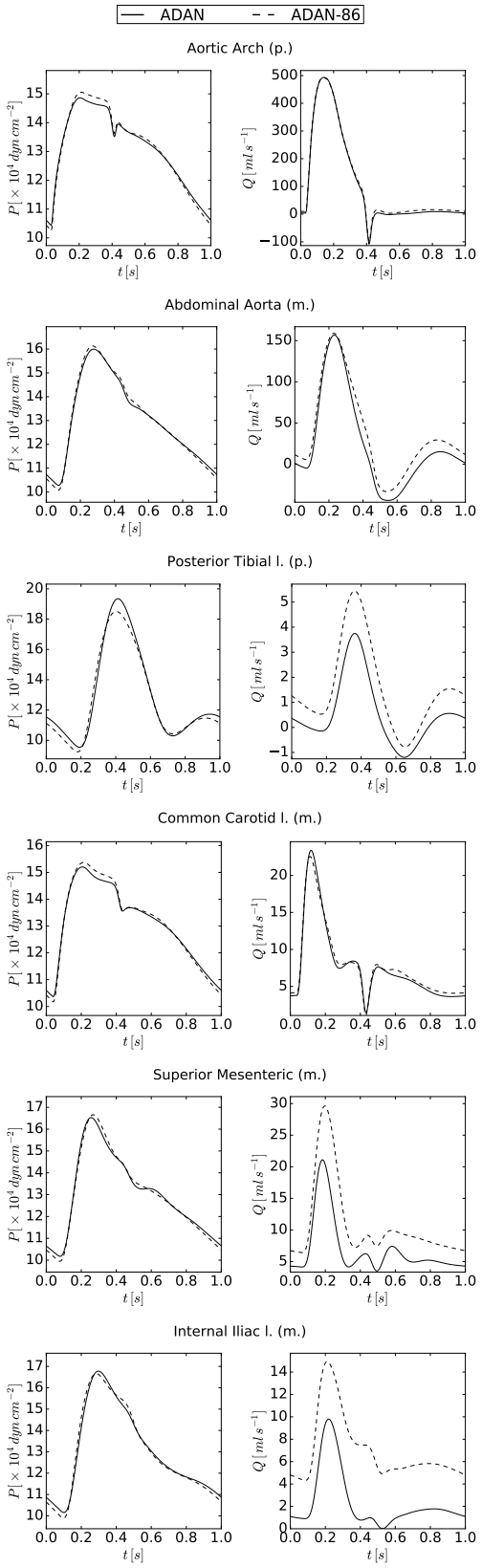

Fig. 3 Pressure (left column) and flow (right column) waveforms for ADAN (solid line) and ADAN-86 (dashed line). p.: proximal location, m.: middle location, l.: left. AoA: aortic arch, AbAo: abdominal aorta, PTA: posterior tibial artery, CCA: common carotid artery, SMA: superior mesenteric artery, IIA: internal iliac artery.

Concerning the blood supply to the brain and extracranial territories, the ADAN model gives an external carotid/internal carotid flow ratio of 0.57, and a common carotid/vertebral flow ratio of 6.72. For the ADAN-86 model these values are 0.59 and 5.96, respectively. In Sato et al (2011) these values are 0.54 and 4.04, respectively.

Figure 4 features the aortic root impedance for both models. Both spectra are rather similar. The difference in the moduli Z/Z_c in the first two harmonics is 15% and 13%, respectively (relative to the average of Z/Z_c over the first 14 harmonics. The discrepancy (relative to the average of the absolute value) in the phase for the first 14 harmonics ranges between -8% (6th) and 36% (3rd), with a mean of 6%.

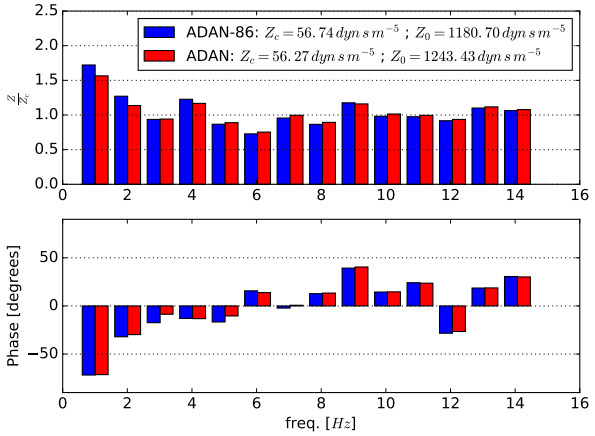

Fig. 4 Aortic root impedance spectrum in modulus and phase for ADAN (red bars) and ADAN-86 (blue bars). Modulus is nondimensionalized by the characteristic impedance Z_c.

Wave intensity for selected central and peripheral vessels, with specific focus in cerebral arteries, is shown in Figure 5, discriminating the contribution of the forward and backward compression and expansion waves: FCW when $du_+ > 0$ and $dp_+ > 0$, FEW when $du_+ < 0$ and $dp_+ < 0$, BCW when $du_- < 0$ and $dp_- > 0$ and BEW when $du_- < 0$ and $dp_- < 0$. At the aortic arch, the wave intensities of both models are very similar. The FCW and FEW are almost identical, while the BCW is slightly larger in the ADAN-86. At the PTA, the FCW in ADAN-86 is larger, while the BCW is stronger in ADAN, and the total energy differs significantly. At the CCA, FCW and BCW are weaker in ADAN, while FEW and BEW are almost identical. For the anterior cerebral artery (ACA) the FCW is weaker in ADAN, but the BCW is slightly larger. And for the posterior communicating artery (PCoA), in both models the energy transfer occurs from the anterior circulation to

the posterior circulation. However, the competition between forward and backward waves differs.

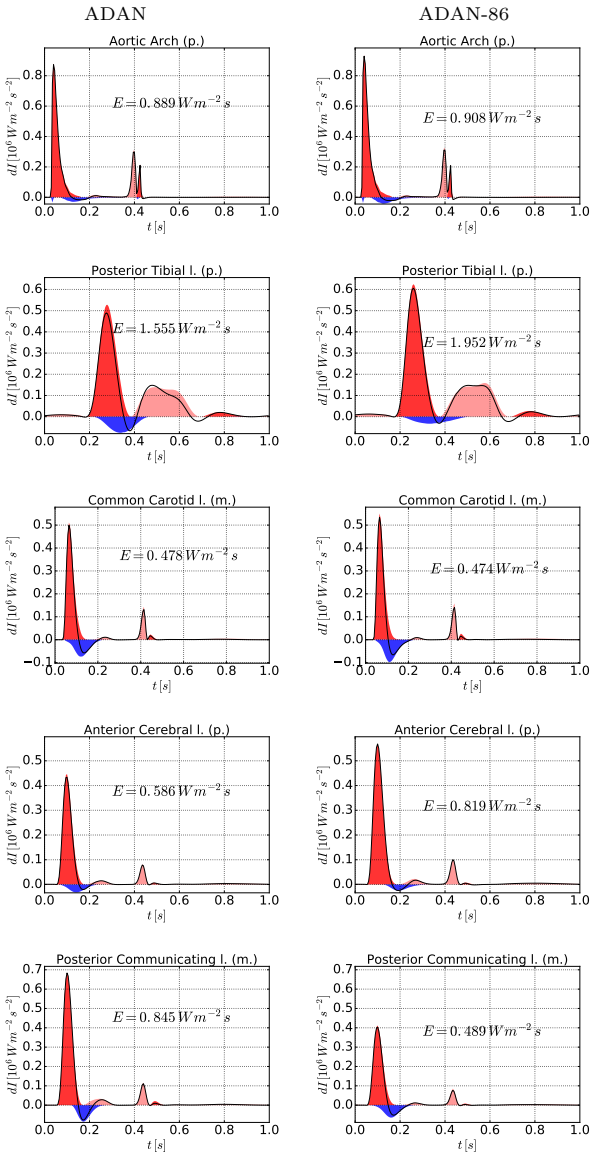

Fig. 5 Wave intensity analysis for ADAN (left) and ADAN-86 (right) at selected locations. Red shaded areas indicate FCW (dark red) and FEW (light red). Blue shaded areas indicate BCW (dark blue) and BEW (light blue). The wave energy over the cardiac cycle is shown in each plot. p.: proximal location, m.: middle location, l.: left. AoA: aortic arch, PTA: posterior tibial artery, CCA: common carotid artery, ACA: anterior cerebral artery, PCoA: posterior communicating artery.

3.2 Left CCA total occlusion

Table 4 (see columns named *w/ACoA*) presents percentage change of mean flow rate in the case of common carotid total occlusion with respect to the corresponding healthy condition for all arteries that supply the head. More specifically: common carotid arteries (CCA), internal carotid arteries (ICA), external carotid arteries (ECA), vertebral arteries (VA), anterior (ACA), middle (MCA) and posterior cerebral arteries (PCA). Alltogether, the ACA, MCA and PCA render the total cerebral blood flow (CBF) reported in the table.

Reduction of CBF in the ADAN-86 model is larger than in the ADAN model. The blood flow in the l. CCA stops in both models (change −100.0%), while the r. CCA in ADAN supplies more blood than in ADAN-86, particularly in the absence of the ACoA (increase of 64.8% vs. 53.5% w/ACoA, 44.8% vs. 8.2% wo/ACoA). At the l. ICA, situated on the same side (ipsilateral) as the occlusion, there is almost no flow rate in ADAN (change −109.9%), while in the ADAN-86 the flow in the same artery is inverted to supply the territories downstream the ipsilateral ECA (change −139.2%). The r. (contralateral) ICA in the ADAN-86 provides more blood to the CoW than in the ADAN model (83.5% vs. 66.4% w/ACoA, 9.7% vs. 12.0% wo/ACoA), and the same observation holds for the l. and r. VA. In the ADAN, the r. ECA increases its flow markedly, while in the ADAN-86 the flow remains almost invariant (62.2% vs. 2.4% w/ACoA, 103.2% vs. 5.5% w/ACoA). The reduction of blood flow in l. and r. ACA and l. and r. MCA are qualitatively similar, although ADAN-86 predicts sharper blood flow reduction. Different qualitative and quantitative behaviors are observed when comparing ADAN and ADAN-86 in the territories supplied by the l. and r. PCA.

Distal to the occlusion, ipsilateral vessels in ADAN present flow and pressure waveforms with different qualitative and quantitative signatures when compared to ADAN-86, as seen in Figure 6. The ipsilateral ICA flow in ADAN is inverted during systole and antegrade during diastole. This inversion is larger in ADAN-86 because of the flow required by the ipsilateral ECA (this explains the flow change above 100% seen in Table 4). The l. ECA flow rate at proximal location is partially inverted during the cardiac cycle, and it is completely inverted distal to thyroid branching vessels in ADAN, while it is completely antegrade in ADAN-86. Regarding the contralateral circulation, the flow in the r. ECA remains invariant in ADAN-86, while in ADAN the same flow is increased (see also Table 4), and the r. ICA features a flow waveform with a larger pulsatility in ADAN. The pressure drop across the occlusion (difference between proximal and distal pressure values, the latter also called wedge pressure), for ADAN and ADAN-86, respectively, is $2.32 \cdot 10^4$ dyn/cm^2 vs.

Territory / Artery	$\Delta\bar{Q}$ [%] w/ACoA				$\Delta\bar{Q}$ [%] wo/ACoA				$\bar{Q}^*$ [cm^3/s]			
	ADAN		ADAN-86		ADAN		ADAN-86		ADAN		ADAN-86	
	l.	r.	l.	r.	l.	r.	l.	r.	l.	r.	l.	r.
CBF	-7.0		-12.0		-11.7		-25.7		10.74		12.61	
CCA	-100.0	64.8	-100.0	53.5	-100.0	44.8	-100.0	8.2	7.68	7.68	7.92	7.92
ICA	-109.9	66.4	-139.2	83.5	-78.2	12.0	-114.9	9.7	4.88	4.91	4.96	4.99
ECA	-82.6	62.2	-34.2	2.4	-138.1	103.2	-75.1	5.5	2.79	2.76	2.96	2.93
VA	56.8	56.7	46.0	45.8	81.6	81.8	74.0	73.9	1.09	1.10	1.33	1.33
ACA	-17.3	-2.9	-25.3	-6.1	-37.8	3.4	-73.7	5.6	1.62	1.62	2.09	2.09
MCA	-14.9	-1.4	-29.7	-1.2	-29.8	1.9	-73.4	5.6	2.67	2.67	2.67	2.67
PCA	2.7	-1.6	-1.9	-0.4	8.5	-4.5	-2.0	1.3	1.08	1.08	1.54	1.54

Table 4 Percentage change of mean blood flow with respect to the reference healthy condition ($\bar{Q}^*$) for total carotid occlusion ($\Delta\bar{Q}$) for ADAN and ADAN-86, with and without anterior communicating artery (w/ACoA and wo/ACoA, respectively). CBF: cerebral blood flow, ICA: internal carotid artery, ECA: external carotid artery, VA: vertebral artery, ACA: anterior cerebral artery, MCA: middle cerebral artery, PCA: posterior cerebral artery, l.: left, r.: right.

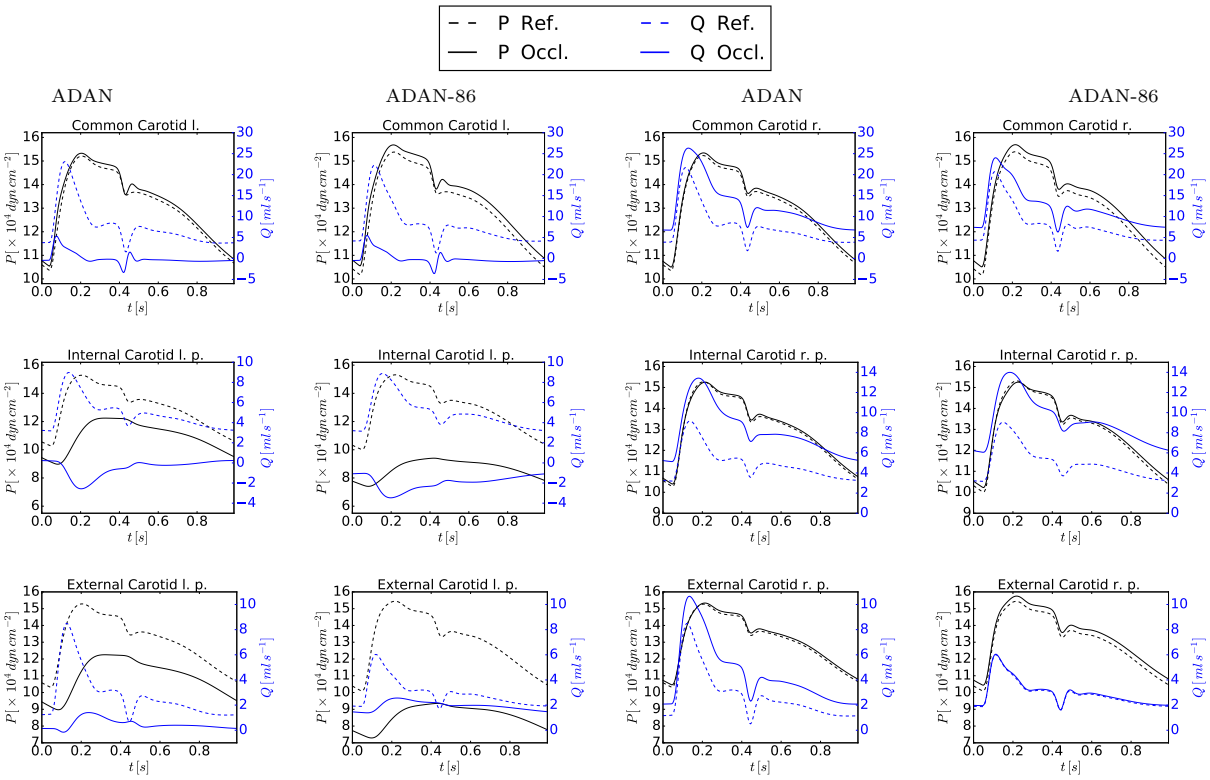

Fig. 6 Pressure (black) and flow rate (blue) waveforms at selected arteries for ADAN (first and third columns) and ADAN-86 (second and fourth columns) for CCA occlusion. Dashed lines: reference scenario. Solid lines: occlusion scenario w/ACoA. l.: left, r.: right, p.: proximal location.

$4.82 \cdot 10^4$ dyn/cm^2 (w/ACoA) and $4.00 \cdot 10^4$ dyn/cm^2 vs. $10.57 \cdot 10^4$ dyn/cm^2 (wo/ACoA).

Wave intensity analysis is presented in Figure 7 at selected vessels distal to the occlusion site. Observe that, because of the CoW, wave intensity is the result of a complex interaction between forward and backward waves. BCW dominates during systole in the ipsilateral ICA, while it competes with systolic FCW at the ipsilateral ECA. These patterns are qualitatively similar, but more pronounced in ADAN than in ADAN-86, and give insight about wave propagation phenomena downstream the occlusion. In the MCA, ADAN model manages to transfer more energy. At the PCoA, qualitative and quantitative differences between ADAN and ADAN-86 are notorious. The contralateral PCoA is more engaged in the collateral circulation in ADAN, carrying more energy.

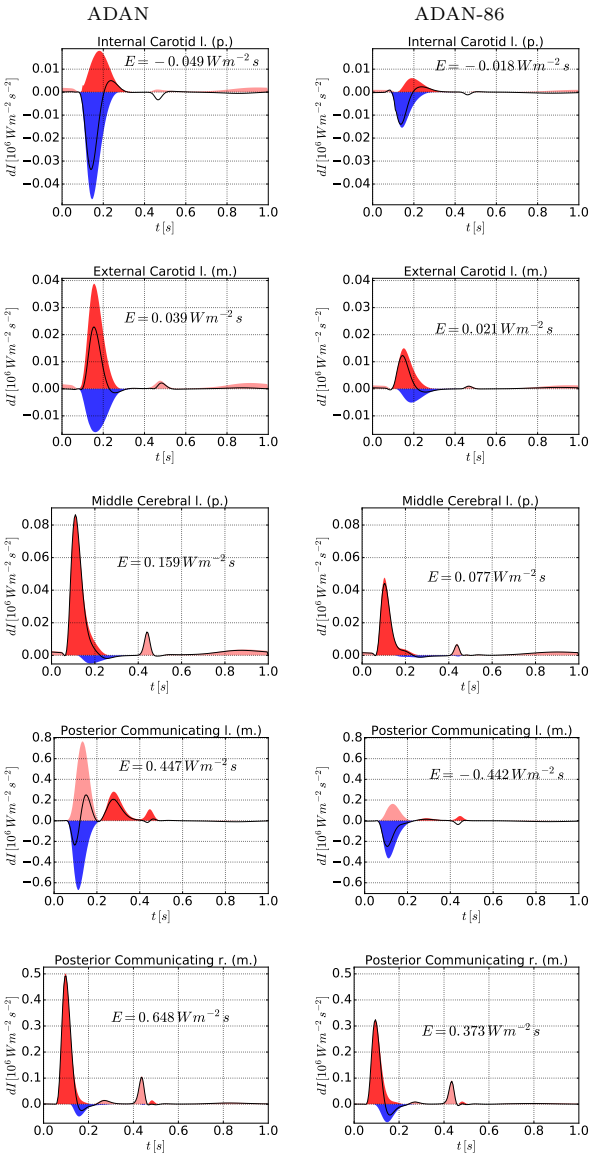

Fig. 7 Wave intensity analysis for ADAN (left) and ADAN-86 (right) at ipsilateral and contralateral selected locations for the case of left CCA occlusion. Red shaded areas indicate FCW (dark red) and FEW (light red). Blue shaded areas indicate BCW (dark blue) and BEW (light blue). The wave energy over the cardiac cycle is shown in each plot. l.: left, r.: right, p.: proximal location, m.: middle location. ICA: internal carotid artery, ECA: external carotid artery, MCA: middle cerebral artery, PCoA: posterior communicating artery.

3.3 Impact of ACoA in CCA total occlusion

We considered an anatomical variation in the CoW, by removing the ACoA. Results are reported in Table 4. When the ACoA is absent, CBF is more affected by the occlusion of the CCA than for the case of a complete CoW. The reduction in the CBF is larger in the ADAN-86. Without the ACoA, both models manage to redistribute the blood supply towards the posterior circulation, increasing the flow in both VAs and reducing the flow in the contralateral CCA because of the reduction of the contralateral ICA blood requirement. Differences between ADAN and ADAN-86 with the ACoA are stressed in the case without ACoA. In the ADAN model, the ipsilateral ECA flow is directed backwards, supplying blood to the ICA. Such ipsilateral ECA flow remains antegrade in ADAN-86. As a result of this, in ADAN the contralateral ECA has to supply the territories downstream the ipsilateral ECA, and therefore there is a remarkable increase in the blood flow in this artery. As for the contralateral cerebral hemisphere (ACA, MCA and PCA), both models predict almost invariance of blood supply.

Without the ACoA, the average pressure difference across the occlusion predicted by both models differs considerably. For ADAN-86 it becomes $10.57{\cdot}10^4$ dyn/cm^2 (increase of 119.6% with respect to the case with ACoA), while for ADAN it is $4.00 \cdot 10^4$ dyn/cm^2 (increase of 72.8% with respect to the case with ACoA).

Figure 8 presents a complementary visualization to the data reported in Table 4, displaying the pressure and flow rate waveforms in the major arteries around the CoW for both networks and for the two scenarios considered, with and without ACoA. These figures feature the sensitivity of each model to the existence of the ACoA. The changes produced by the anterior collateralization differ substantially in ADAN and ADAN-86 in the ipsilateral vessels, while the discrepancies are moderate in contralateral arteries. For example, the flow rate through the MCA is less affected in ADAN, because of the more effective engagement of the left PCoA. The contralateral ECA significantly contributes to the cross-filling of extra-cranial territories through facial collateral vessels, as observed in the vessels lighted in Figure 9. In such figure the comparison is performed similarly to that from Table 4, that is, we report the flow change $Q_{\text{ref}} - Q_{\text{occ}}$ relative to a characteristic flow rate $Q^* = 5$ cm^3/s.

4 Discussion

4.1 Healthy model

Differences between solutions obtained with both models for the healthy condition were qualitatively and quantitatively characterized. Similarities in central vessels are explained by the fact that one model (ADAN-86) is the truncation of the other (ADAN), sharing the same values of many model parameters. Major differences are caused by the different topological arrangement of vessels, which are stressed in pathological conditions. The simple algebraic procedure to define terminal models

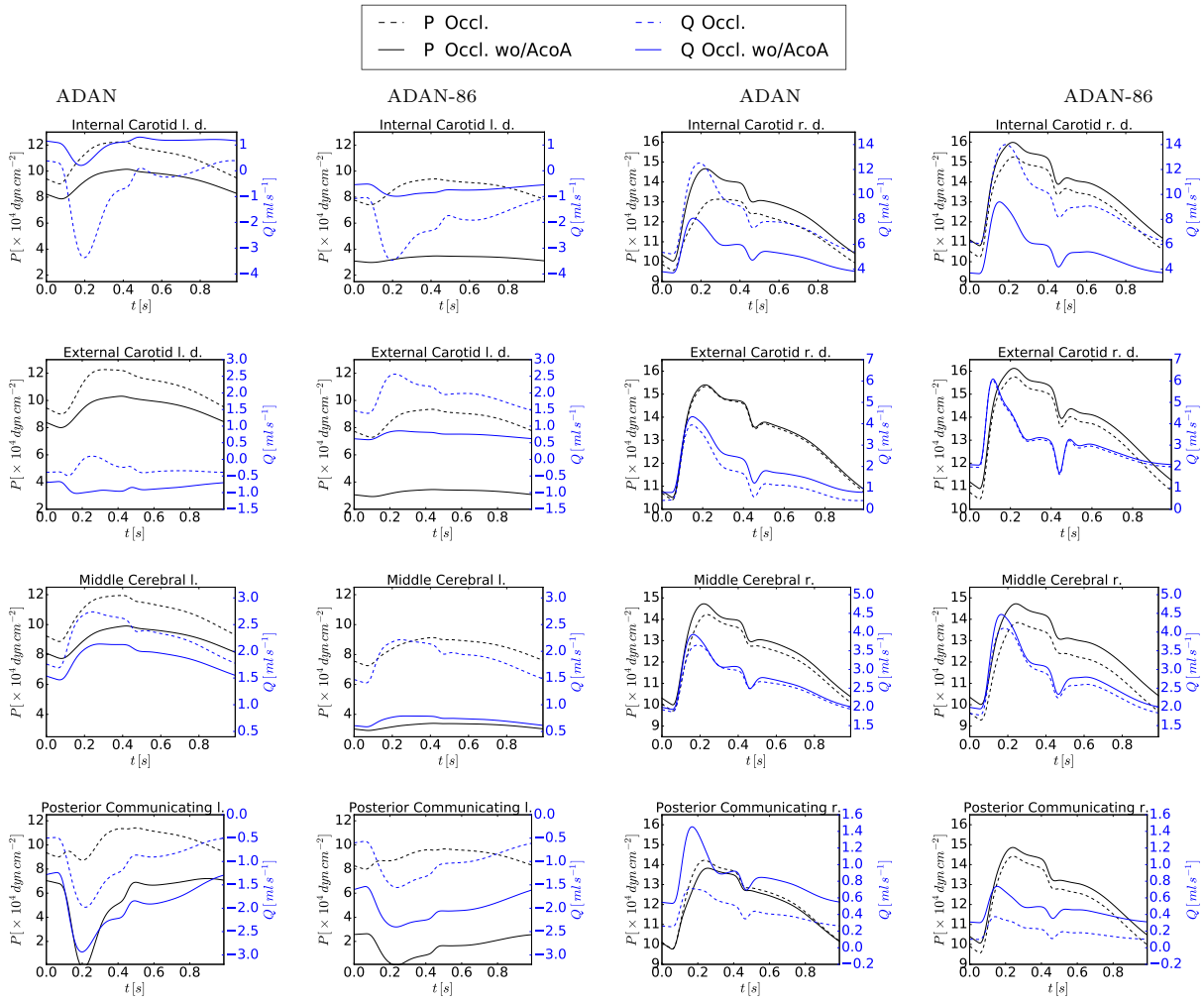

Fig. 8 Pressure (black) and flow rate (blue) waveforms at selected cerebral arteries for ADAN (first and third columns) and ADAN-86 (second and fourth columns). Dashed lines: CCA occlusion with ACoA. Solid lines: CCA occlusion wo/ACoA. l.: left, r.: right, d.: proximal location. ICA: internal carotid artery, ECA: external carotid artery, MCA: middle cerebral artery, PCoA: posterior communicating artery.

would explain only minor discrepancies encountered at distal locations (Fossan et al, 2018). In fact, we have implemented the strategy to define ratio between terminal resistances proposed in Epstein et al (2015) (results not reported here), and the differences were not significant, which strenghtens the conclusion that significant differences are caused by the anatomical refinement in the model and the consequent mismatch in the blood supply to territories.

Overall, the disagreement in the pressure waveform is rather small. However, even when pressure differences are small, large deviations in the flow rate can be observed.

In many vessels differences in flow rate are the result of blood excess (caused by missing territories in ADAN-86) sent to upper and lower limbs. Such blood overload conducted through terminal tapered vessels slightly affects the pressure contour at the ascending aorta, but these discrepancies are augmented as we move towards distal territories, where the anatomical definition in ADAN-86 is poorer (see Figure 3). In vessels such as the SMA, ADAN-86 predicts a flow rate contour resembling a low-resistance downstream territory, while ADAN predicts a flow signal which is the typical (high-resistance) signature for these vessels Geelkerken et al (1998); Osada et al (2007). Such divergent behavior is explained by the complex blood delivery system to the intestines as given by the inferior and superior mesenteric arteries, with anastomoses occurring between proximal and distal sites of these vessels through the middle colic artery, the ascending colic artery and the marginal artery of intestine. The closest connection between arterial vessels and vascular territories reduces the impact of modeling assumptions (specifically outflow conditions), predict-

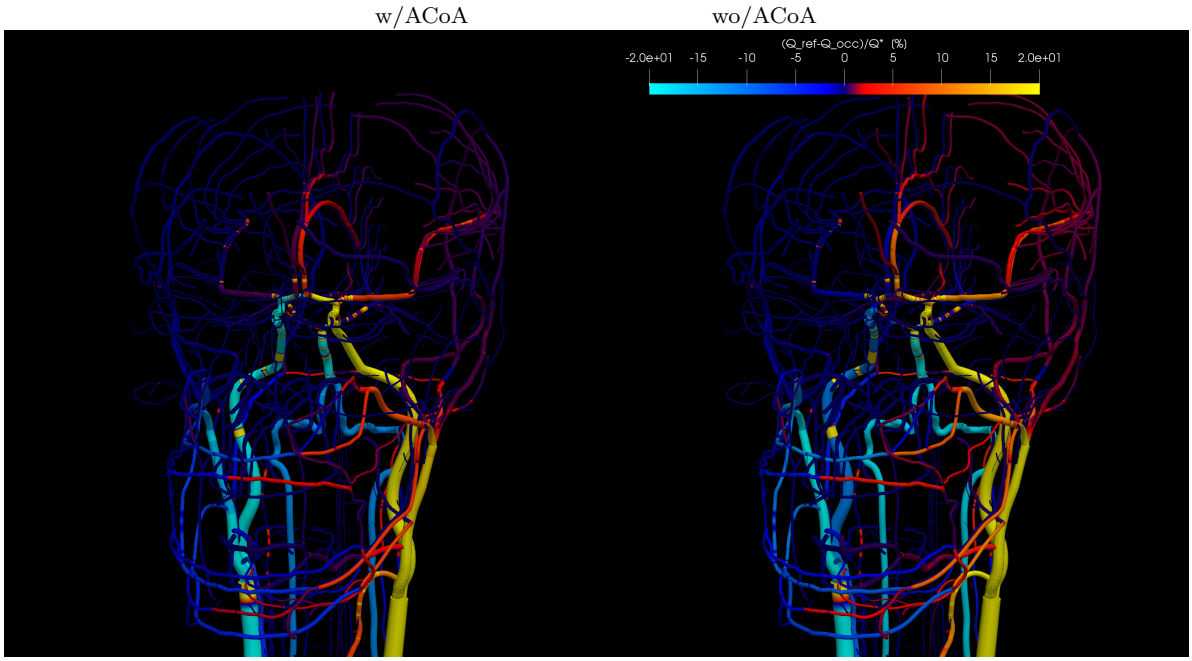

Fig. 9 Laterofrontal view of the vasculature in the head in ADAN model. Alteration (%) in the mean blood flow with respect to the reference condition for cases with ACoA (left) and without ACoA (right). The scale ranges from -20% to 20%, using a normalization flow rate value $Q^* = 5$ cm^3/s.

ing a more physiologically realistic hemodynamic environment in peripheral vessels.

Essential cardiovascular features, such as impedance spectrum at the aortic root as well as the ABI and PWV indexes, are very similar in both models. In this sense, simplified models provide a reliable (and cheaper) tool to quantify arterial function Avolio et al (2009); Heald et al (2006); O'Rourke and Hashimoto (2007).

Concerning the blood supply to the brain, in the reference scenario both models predict the hemodynamics environment well not only in the major vessels supplying the brain, but also in the flow transported by the vessels in the anterior and posterior neck circulations.

The present findings agree with those reported in Guan et al (2016), where, by comparing structured-tree and Windkessel terminal representations, the authors found high sensitivity in the predictions to the choice of the terminal model. As in the present work, this suggests that the truncation of the vascular network introduces significant deviations at both peripheral locations and in pathological conditions.

4.2 Left CCA total occlusion

In the case of CCA occlusion, the hemodynamic environment in the brain in ADAN is less affected than in ADAN-86. The lack of collateral vessels other than those provided by the CoW in ADAN-86 precludes blood from reaching the brain, with a consequent larger reduction in CBF. In ADAN, the presence of extracranial vessels and collaterals in the anterior and posterior circulations helps to increment flow reserve and to carry more blood to the brain in such pathological condition. The pressure drop across the occlusion in ADAN-86 is nearly 90% larger than the value given by ADAN, and flow rate through ipsilateral ACA and MCA drop much more in ADAN-86. In addition, ADAN predicts a small steal phenomena (flow increase) occurring at the PCAs, in contrast to the reduction predicted by ADAN-86.

Flow waveforms are remarkably different at the ECA and ICA. The pressure waveform distal to the occlusion in ADAN-86 is blunter than in ADAN. This is caused by discrepancies in the downstream and upstream impedances at each reflecting point (bifurcations), which are the consequence of the network topology.

Concerning the flow contour in the ipsilateral ICA, ADAN predicts a bidirectional flow, with antegrade flow during diastole and flow inversion during systole, which is the result of a fluctuating gradient of hemodynamic forces during the cardiac cycle. Instead, ADAN-86 predicts a fully retrograde flow, which is the consequence of the blood request imposed by the distal territories of the ipsilateral ECA. Such behavior is recognized as *carotid steal phenomenon* Ozbek et al (1998); Toole and McGraw (1975), and has been widely reported in the literature with contradictory findings concerning whether

the steal is ICA-to-ECA Ouriel et al (2001) (flow from ICA into ECA) or ECA-to-ICA Ozbek et al (1998) (flow from ECA into ICA).

According to Ouriel et al (2001); Tindall et al (1963), in most cases, ipsilateral ICA systolic flow is retrograde and diastolic flow is antegrade, just as predicted by the ADAN model (i.e. ICA-to-ECA partial steal). In turn, ADAN-86 will always predict a full retrograde flow because the ipsilateral ECA can uniquely be fed through the CoW-ICA complex.

At the l. ECA, in contrast to ADAN-86, ADAN shows an almost total reduction of flow, with inversion during diastole. This is because ipsilateral downstream territories of the ECA are mostly supplied by distal collateral pathways, thus avoiding an exaggerated burden to the l. ICA. As a result, the r. ECA in ADAN compensates this reduction by carrying blood to these territories, a mechanism that cannot be activated in ADAN-86, where r. ECA flow remains almost invariant.

In view of the striking similarities in the predictions delivered by ADAN and ADAN-86 discussed in the previous section for the reference condition, it must be highlighted that the differences observed in the presence of disease could be mitigated through the construction of a modified reduced model specifically tailored to match predictions of ADAN. That is, ADAN can guide the development of a modified vascular network with respect to ADAN-86 in order to account for the specific phenomenology observed in such abnormal conditions.

4.3 Impact of ACoA in CCA total occlusion

Collateral circulation in the brain is a fundamental contributing factor to determine mechanisms involved in the onset and progress of cerebrovascular diseases. Although anatomical knowledge of collateral pathways can help to determine risk of cerebral ischemia and thus to guide and improve therapeutic strategies, it remains largely underused in the specialized literature Liebeskind (2003). In this context, the anatomically detailed arterial topology of the ADAN model is capable of shedding light on the mechanisms triggering collateral circulation pathways and their functional impact in cerebral blood flow. Moreover, studies with personalized anatomical definition (CoW characterized by medical images) may contribute to improve the understanding of surgical outcomes in a patient-specific scenario.

The quantitative analysis presented in Table 4 (see case without ACoA, and compare also with ACoA) demonstrates that a very subtle perturbation in the vascular anatomy (absence of ACoA) produces a large functional variability of primary vessels supplying the extracranial and intracranial territories. More importantly, in the case of incomplete CoW, hemodynamic changes predicted by ADAN-86 diverge from those given by ADAN. In other words, in the case of disease (CCA occlusion), discrepancies between models are larger. Indeed, ADAN-86 predicts a reduction in CBF which doubles the reduction observed in ADAN. Unlike ADAN, the absence of the ACoA in ADAN-86 makes the r. CCA almost insensitive to the occlusion, while both VA almost double the amount of blood that they carry.

Specifically focusing in the analysis of ICA-ECA steal phenomena in the case of CCA occlusion, consensus in the literature dictates that ICA-to-ECA partial steal (i.e. partial inversion of ICA flow) occurs when favourable interhemispheric cross-filling conditions exist at the CoW through the ACoA, while ECA-to-ICA steal takes place in cases of incomplete CoW, e.g. when the ACoA is absent Dorrance (1934); Liebeskind (2003). In the simulated cases without the ACoA, the ipsilateral ECA in ADAN presents complete inversion of flow distally to thyroid branches, and partial inversion at proximal locations, that is, a complete ECA-to-ICA steal phenomenon is observed when considering vessels supplying the upper part of the head. Consequently, the l. ICA flow is fully antegrade in ADAN. Moreover, collateral vessels in the extracranial territories formed by thyroidal vessels, angular arteries and nasal arteries, among others also contribute to supply the CoW through the ECA-ICA pathway. Such cross-filling is provided by the r. ECA, whose flow is markedly augmented in ADAN. Concerning cerebral flow, the ipsilateral hemispheric blood flow is far less reduced in ADAN than in ADAN-86, and the steal phenomena occurring in the posterior circulation is more pronounced than in the case with ACoA.

In both models, when the ACoA is present, flow is delivered from contralateral to ipsilateral ICA through the ACoA. Thus, we have inverted flow in the proximal part of the ipsilateral ACA, as well as the important contribution provided by the ipsilateral PCoA, inverting its flow with respect to the healthy condition. The same inversion is noted in the contralateral PCoA. Outgoing vessels of the CoW feature different flow change for both scenarios (with and without ACoA). When the ACoA is present, contralateral ACA, MCA and PCA territories have light reduction of blood supply. In contrast, when ACoA is absent, the contralateral ACA and MCA territories increase flow, and the contralateral PCA territory now reduces its flow in ADAN. This is remarkable because in such case the increase of flow in l. and r. VA, is more pronounced than in the case with ACoA. That is, a posterior interhemispheric

steal phenomenon is taking place. Also, ADAN predicts that ipsilateral ACA is the most compromised vessel when ACoA is not present, while ADAN-86 predicts that both ACA and MCA are equally affected. This is because of the important function of the PCoA, as said above.

From the purely anatomical point of view, extracranial collaterals encompass crossing anastomoses corresponding to the thyroid arterial plexus, laryngeal, facial and occipital arteries. Flow through most of all these arteries features contralateral increase and ipsilateral inversion, providing a protective mechanisms to cope with occlusions in major vessels.

Here, we could appreciate that the presence of an occlusion triggers a complex interaction of hemodynamic forces. The phenomenology observed in ADAN-86 and ADAN models differs significantly. These differences are emphasized in the case with an open CoW (without ACoA). In ADAN, blood manages to reach the brain more easily because of the existence of extracranial collaterals near facial and neck territories. This is extraordinary, and is an unprecedented proof-of-concept that subtle anatomic variations are able to activate quite different collateral mechanisms of blood supply, and such subtle variations can determine, for instance, the direction of the ICA flow, which is of the utmost importance in protective occlusion procedures Ouriel et al (2001).

As discussed, model predictions provide solid foundations to observations available in the specialized literature Ouriel et al (2001); Ozbek et al (1998), as well as to purely anatomy-based inference Dorrance (1934). One of the clear advantages of this kind of study is that it provides extremely rich insight into the balance of hemodynamic forces that determine blood supply to vascular territories, both in health and disease.

4.4 Limitations

Concerning the simulation of total CCA occlusion, collateralization through the pial network has not been considered in ADAN model. This could be regarded as a limitation in assessing the CBF in such pathological condition, because of the reactivity of these vessels and vasodilatory effect which certainly contributes with additional cerebral flow reserve. Assessing the role of these collaterals remains an open issue up to the authors' knowledge.

In the present study we have neglected the cardiac function because the focus was on arterial function. However, cardiac-arterial coupling is expected to bring both models to different equilibrium points in terms of inflow condition. Such interaction is more relevant when analyzing the sensitivity of the equilibrium point as a consequence of introducing perturbations at the systemic level. Previous studies addressed such important question, and discussed the interaction among heart mechanics and arterial circulation when abnormal conditions at the systemic level are encountered, for example in hypertension or aging modeling Liang et al (2009); Segers et al (2001). In contrast, in the case of arterial occlusion and collateral analysis in the brain, where abnormal conditions are restricted to specific vessels, cardiac-arterial coupling is believed to have little effect.

In the case of CCA occlusion, it has been acknowledged that the vasodilatory capacity of brain vessels in the affected hemisphere is abnormal Bokkers et al (2011). The increase in radius would in turn affect arterial stiffness. However, results not reported here accounting for vasodilatory compensation (reduction of cerebral vascular resistance to maintain CBF) and increased vessel stiffness (elastic moduli $\times 2$) have shown that the above discussion remains valid.

5 Conclusions

A quantitative and qualitative comparison between an anatomically detailed arterial network (ADAN) model and a simplified network with commonly used anatomical detail has been presented. Comparisons were made for healthy conditions and for the case of common carotid artery occlusion.

In the healthy condition, the sensitivity of arterial pressure contours to the level of anatomical definition is rather low compared to the sensitivity observed in flow rate waveforms. Differences in pressure are mainly due to strong reflections at bifurcations and at tapered terminal vessels in the simplified model. The effect of these reflections can also be noticed in global characteristics of the model, such as cardiovascular indexes and input network impedance.

Discrepancies in flow rate are significantly larger, and pose the debate on top of the outflow boundary conditions in truncated networks. In this context, an advantage of the ADAN model is the direct connection of the arterial network with vascular territories, reducing the impact of modeling assumptions. The same considerations are valid for wave intensity analysis, in which differences are small in major vessels and become significant towards the periphery and even more accentuated in the case of disease.

In the case of common carotid occlusion, the agreement between both model predictions rapidly deteriorates, with even larger differences for a scenario where an anatomical variation in the Circle of Willis is considered. Here, the ADAN model can rationally explain

intricate steal mechanisms occurring between extracranial and intracranial vasculatures, as well as from contralateral to ipsilateral vessels. It was shown that hemodynamic forces coexist in a weak equilibrium dictated by anatomy, in the sense that subtle anatomic perturbations promote the activation of different collateral pathways.

On the one hand, we conclude that the study of systemic indexes relying on the overall circulation can reasonably be modeled using anatomically simplified networks. On the other hand, highly detailed models like ADAN provide an unprecedented rational mechanistic approach to test medical hypotheses and prove (or refute) conjectures concerning hemodynamics in the case of health and, more importantly, disease. This turns to be of relevance when studying intricate circulatory mechanisms triggered mainly in the case of disease.

Acknowledgements

This work was partially supported by the Brazilian agencies CNPq and FAPERJ. The support of these agencies is gratefully acknowledged.

References

Alastruey J, Parker K, Peiró J, Byrd S, Sherwin S (2007) Modelling the circle of Willis to assess the effects of anatomical variations and occlusions on cerebral flows. J Biomech 40:1794–1805

Alastruey J, Hunt A, Weinberg P (2014) Novel wave intensity analysis of arterial pulse wave propagation accounting for peripheral reflections. Ann Biomed Engng 30:249–279

Armentano R, Levenson J, Barra J, Cabrera E, Breitbart G, Pichel R, Simon A (1991) Assessment of elastin and collagen contribution to aortic elasticity in concious dogs. Am J Physiol Heart Circ Physiol 260:H1870–H1877

Avolio A (1980) Multi-branched model of the human arterial system. Med Biol Eng Comput 18:709–718

Avolio A, Van Bortel L, Boutouyrie P, Cockcroft J, McEniery C, Protogerou A, Roman M, Safar M, Segers P, Smulyan H (2009) Role of pulse pressure amplification in arterial hypertension: experts' opinion and review of the data. Hypertension 54:375–383

Blanco P, Watanabe S, Dari E, Passos M, Feijóo R (2014) Blood flow distribution in an anatomically detailed arterial network model: criteria and algorithm. Biomechanics and Modeling in Mechanobiology 13:1303–1330

Blanco P, Watanabe S, Passos M, Lemos P, Feijóo R (2015) An anatomically detailed arterial network model for one-dimensional computational hemodynamics. IEEE Transactions on Biomedical Engineering 62:736–753

Blanco P, Müller L, Watanabe S, Feijóo R (2016) Computational modeling of blood flow steal phenomena caused by subclavian stenoses. Journal of Biomechanics 49(9):1593–1600

Blanco PJ, Müller LO, Spence JD (2017) Blood pressure gradients in cerebral arteries: a clue to pathogenesis of cerebral small vessel disease. Stroke and Vascular Neurology 3:e000,087

Bokkers R, Wessels F, van der Worp H, Zwanenburg J, Mali W, Hendrikse J (2011) Vasodilatory capacity of the cerebral vasculature in patients with carotid artery stenosis. AJNR Am J Neuroradiol 32:1030–1033

Burton A (1954) Relation of structure to function of the tissues of the wall of blood vessels. Physiol Rev 34:619–642

Dauber W (2007) Pocket Atlas of Human Anatomy by Feneis, 5th edn. Thieme

Dorrance G (1934) Ligation of the great vessels of the neck. Annals of Surgery 99:721–742

Epstein S, Willemet M, Chowienczyk P, Alastruey J (2015) Reducing the number of parameters in 1d arterial blood flow modeling: less is more for patient-specific simulations. Am J Physiol Heart Circ Physiol 309:H222–H234

Fossan FE, Mariscal-Harana J, Alastruey J, Hellevik LR (2018) Optimization of topological complexity for one-dimensional arterial blood flow models. Journal of The Royal Society Interface 15(149):20180,546

Geelkerken RH, Lamers CB, Delahunt TA, Hermans J, Zwijsen JH, van Bockel J (1998) Duodenal meal stimulation leads to coeliac artery vasoconstriction and superior mesenteric artery vasodilatation: an intra-abdominal ultrasound study. Ultrasound in Medicine & Biology 24(9):1351–1356

Godlevska M, Slutskii L, Purinya B (1974) Comparison of the mechanical and biochemical characteristics of human brain arteries. Polymer mechanics 10:941–949

Guan D, Liang F, Gremaud PA (2016) Comparison of the windkessel model and structured-tree model applied to prescribe outflow boundary conditions for a one-dimensional arterial tree model. Journal of Biomechanics 49(9):1583–1592

Heald C, Fowkes F, Murray G, Price J (2006) Risk of mortality and cardiovascular disease associated with the ankle-brachial index: Systematic review. Atherosclerosis 189:61–69

HeMoLab (2013) ADAN-WEB application. Url: http://hemolab.lncc.br/adan-web

Ho H, McGhee C, Hunter P (2012) Numerical analysis for the blood flow in a patient-specific ophthalmic artery. Medical Engineering and Physics 34:123–127

Jianu A, Motoc A, Mihai A, Rusu M (2009) An anatomical study of the thyroid arteries anastomoses. Romanian Journal of Morphology and Embryology 50:97–101

Koeppl T, Schneider M, Pohl U, Wohlmuth B (2014) The influence of an unilateral carotid artery stenosis on brain oxygenation. Medical Engineering and Physics 36:905–914

Liang F, Takagi S, Himeno R, Liu H (2009) Biomechanical characterization of ventriculararterial coupling during aging: A multi-scale model study. Journal of Biomechanics 42(6):692–704

Liang F, Fukasaku K, Liu H, Takagi S (2011) A computational model study of the influence of the anatomy of the circle of willis on cerebral hyperperfusion following carotid artery surgery. BioMedical Engineering OnLine 10:84

Liebeskind D (2003) Collateral circulation. Stroke 34:2279–2284

Matthys K, Alastruey J, Peiró J, Khir A, Segers P, Verdonck P, Parker K, Sherwin S (2007) Pulse wave propagation in a model human arterial network: Assessment of 1-D numerical simulations against in vitro measurements. J Biomech 40:3476–3486

Müller L, Blanco P, Watanabe S, Feijóo R (2016) A high-order local time stepping finite volume solver for one-dimensional blood flow simulations: application to the ADAN model. Int J Num Meth Biomed Engng 32:e02,761

Müller L, Toro E (2014a) Enhanced global mathematical model for studying cerebral venous blood flow. J Biomech 47:3361–3372

Müller L, Toro E (2014b) A global multiscale mathematical model for the human circulation with emphasis on the venous system. Int J Num Meth Biomed Engng 30:681–725

Mynard J, Nithiarasu P (2008) A 1d arterial blood flow model incorporating ventricular pressure, aortic valve and regional coronary flow using the locally conservative Galerkin (LCG) method. Comm Numer Methods 24:367–417

Mynard J, Smolich J (2015) One-dimensional haemodynamic modeling and wave dynamics in the entire adult circulation. Ann Biomed Engng 43:1443–1460

Mynard J, Davidson M, Penny D, Smolich J (2012) Non-linear separation of pressure, velocity and wave intensity into forward and backward components. Med Biol Eng Comput 50:641–648

Netter F (2011) Atlas of Human Anatomy, 5th edn. Elsevier

Olufsen M, Peskin C, Kim W, Pedersen E, Nadim A, Larsen J (2000) Numerical simulation and experimental validation of blood flow in arteries with structured-tree outflow conditions. Ann Biomed Engng 28:1281–1299

Osada T, Murase N, Kime R, Shiroishi K, Shimomura K, Nagata H, Katsumura T (2007) Arterial blood flow of all abdominal-pelvic organs using Doppler ultrasound: range, variability and physiological impact. Physiological Measurement 28(10):1303–1316

O'Rourke M, Hashimoto J (2007) Mechanical factors in arterial aging: A clinical perspective. Journal of the American College of Cardiology 50:1–13

Ouriel K, Greenberg R, Sarac T (2001) Hemodynamic conditions at the carotid bifurcation during protective common carotid occlusion. Journal of Vascular Surgery 34:577–580

Ozbek S, Killi AMR, Pourbagher M, Demirpolat G, Oran I, Pourbagher A (1998) Carotid steal: report of ten cases. Journal of Ultrasound in Medicine 17:623–629

Perdikaris P, Grinberg L, Karniadakis GE (2015) An effective fractal-tree closure model for simulating blood flow in large arterial networks. Annals of Biomedical Engineering 43(6):1432–1442

Ramsey MW, Sugawara M (1997) Arterial wave intensity and ventriculoarterial interaction. Heart Vessels Suppl 12:128–134

Reymond P, Merenda F, Perren F, Rüfenacht D, Stergiopulos N (2009) Validation of a one-dimensional model of the systemic arterial tree. Am J Physiol Heart Circ Physiol 297:H208–H222

Safaei S, Bradley CP, Suresh V, Mithraratne K, Muller A, Ho H, Ladd D, Hellevik LR, Omholt SW, Chase JG, Müller LO, Watanabe SM, Blanco PJ, de Bono B, Hunter PJ (2016) Roadmap for cardiovascular circulation model: Roadmap for cardiovascular circulation model. The Journal of Physiology 594:6909–6928

Safaei S, Blanco PJ, Müller LO, Hellevik LR, Hunter PJ (2018) Bond Graph Model of Cerebral Circulation: Toward Clinically Feasible Systemic Blood Flow Simulations. Frontiers in Physiology 9:148

Sato K, Ogoh1 S, Hirasawa A, Oue A, Sadamoto T (2011) The distribution of blood flow in the carotid and vertebral arteries during dynamic exercise in humans. The Journal of Physiology 589.11:2847–2856

Segers P, Stergiopulos N, Verdonck P, Westerhof N (2001) Mathematical model analysis of heart-arterial interaction in hypertension. In: 2001 Conference Proceedings of the 23rd Annual International Conference of the IEEE Engineering in Medicine and Biology So-

ciety, vol 1, pp 192–195 vol.1
Stergiopulos N, Young D, Rogge T (1992) Computer simulation of arterial flow with applications to arterial and aortic stenoses. J Biomech 25:1477–1488
Tindall G, Odom G, Dillon M, Jr HC, Jr MM, Jr JG (1963) Direction of blood flow in the internal and external carotid arteries following occlusion of the ipsilateral common carotid artery. Observation in 19 patients. Journal of Neurosurgery 20:985–994
Toole J, McGraw C (1975) The steal syndromes. Annual Review of Medicine 26:321–329
Urquiza S, Desimone H, Goñi M, Introzzi A, Clara F (1995) Prediction of human arterial pulse wave shape changes in aging and hypertension. In: Computer simulations in biomedicine. H. Power, R.T. Hart, S. Hosoda et al. eds., Milan, Italy, pp 131–138
Wang J, Parker K (2004) Wave propagation in a model of the arterial circulation. J Biomech 37:457–470
Weizsacker H, Pinto J (1988) Isotropy and anisotropy of the arterial wall. Journal of biomechanics 21:477–487